Available online www.jocpr.com

Journal of Chemical and Pharmaceutical Research, 2016, 8(2):448-469

Research Article

ISSN : 0975-7384
CODEN(USA) : JCPRC5

Microrobots propulsion system design for drug delivery

M. Y. Abdollahzadeh Jamalabadi[1,2]

[1]*Department of Mechanical, Robotics and Energy Engineering, Dongguk University, 30 Pildong-ro 1gil, Jung-gu, Seoul 100-715, Republic of Korea*
[2]*Chabahar Maritime University, Chabahar, Iran*

ABSTRACT

Scale down robots with propeller propulsion mechanisms are promising tools for minimally invasive surgery, diagnosis, targeted therapy, drug delivery and removing material from human body. Understanding the movement of micro robots inside fluid-filled channels is essential for design and control of reduced robots inside arteries and conduits of living organisms. Three-dimensional governing partial differential equations of the fluid flow, Stokes equations, are solved with computational fluid dynamics (CFD) to predict velocities of robots, which are compared with experiments for validation, and to analyze effects of blade number, pitch and the radial position of the robot on its swimming speed, forces acting on the robot and efficiency.

Keywords: computational fluid dynamics, artery, low Reynolds number, micro-robots

---

INTRODUCTION

Someday, treating patients with nanorobots could become standard practice to deliver medicine specifically to parts of the body affected by disease. But merely injecting drug-loaded nanoparticles might not always be enough to get them where they need to go. Tiny robots could have many benefits for patients. For example, they could be programmed to specifically wipe out cancer cells, which would lower the risk of complications, reduce the need for invasive surgery and lead to faster recoveries. It's a burgeoning field of study with early-stage models currently in development in laboratories. But one of the challenges to making these robots work well is getting them to move through body fluids, which are like molasses to something as small as a Nano robot. Bradley J. Nelson, Salvador Pané, Yizharor and colleagues wanted to address this problem. The researchers strung together three links in a chain about as long as a silk fiber is wide. One segment was a polymer, and two were magnetic, metallic nanowires. They put the tiny devices in a fluid even thicker than blood. And when they applied an oscillating magnetic field, the Nano swimmer moved in an S-like, un-dilatory motion at the speed of nearly one body length per second. The magnetic field also can direct the swimmers to reach targets.

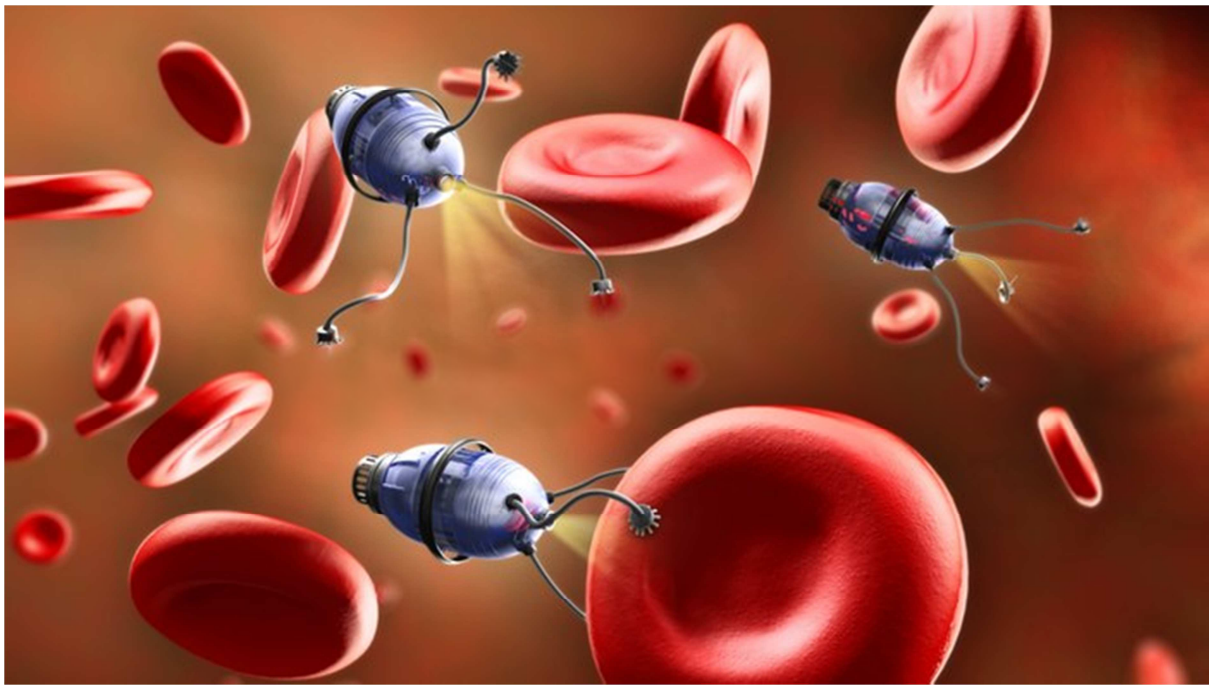

Fig. 1.nanorobots capable of moving through bodily fluids with relative ease [1]

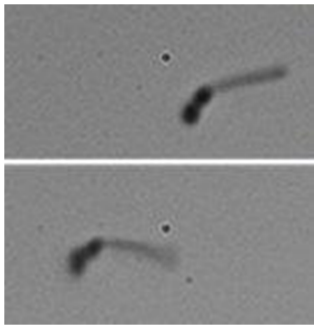

Fig. 2.Patients could one day benefit from swimming nanorobots that deliver drugs where they're needed [2]

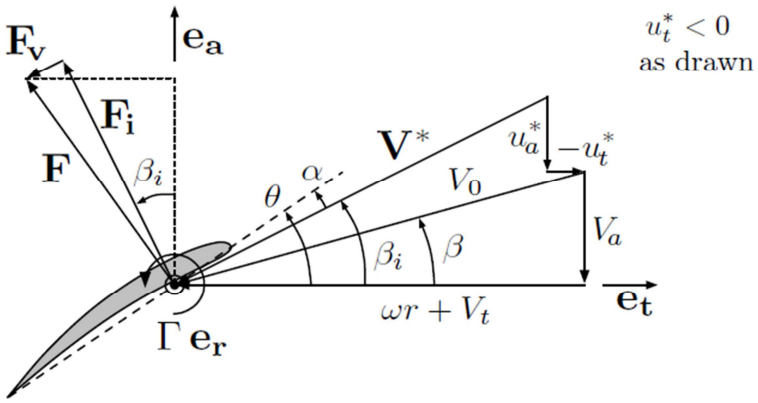

Fig. 3.Propeller velocity and force diagram (per unit span), as viewed from the tip towards the root of the blade on a 2D blade section in the axial e_a and tangential e_t directions.All velocities are relative to a stationary blade section at radius r

.

Miniaturized swimming robots have great potential to revolutionize modern medicine; risks of many life-threatening operations and procedures can be reduced significantly. For instance, potent drugs can be delivered to target organs, tissues and cells; arterial build-up can be removed to enhance blood flow in vital organs; diagnostic information can be collected and delivered from directly within organs and tissues, etc. A comprehensive survey of development of micro robots and their potential impact in medicine is provided by Nelson *et al*. [1].

Propulsion mechanisms of macro scale objects in fluids are inadequate in micro scales where Reynolds number is smaller than 1 and viscous forces dominate. Purcell's scallop theorem demonstrates that a standard propeller is useless for propulsion in micro scales [1]. However, microscopic organisms such as bacteria and spermatozoa can move up to speeds around tens of body lengths per second [2,3, 4] with propulsion generated by their flagellar structures, which are either rotating helices or flexible filaments that undergo un-dilatory motion. Natural microorganisms with helical body, such *Escherichia coli* (cell body is approximately 1×2µm with flagella in 20 nm in diameter and about 8 µm in length) exhibit run-and-tumble behavior that resembles to random walk of a Brownian particle [2]: they swim in nearly linear trajectories (run) interrupted by erratic rotation of the cell in place (tumble) caused by reversing the direction of the rotation of the flagella.

Some microorganisms such as *Escherichia coli* and *Vibrio alginolyticus* use their helical flagella for propulsion in aqueous solutions; a typical organism uses a molecular motor inside the body to generate the torque required to rotate the flagellum. Micro-scale control strategies for flagellated bacteria are demonstrated chemically [1] and magnetically [2]. Martel [3] presents a de-bodied review and list of demonstrations of magneto tactic bacteria as controllable micro and Nano robots inside micro vessels and capillaries as small as 5 µm inside the body [4].

In-channel experiments and modeling studies are necessary to understand the motion and optimization of micro robots inside capillaries and blood vessels. A number of studies in literature report experiments with *E.coli* in channels and capillaries [2]. These results are significant in showing hydrodynamic effects play an important role in swimming of bacteria in channels, and flagellar actuation mechanism is very effective even in narrow channels compared to the size of the organism. Molecular interaction forces between the swimmers and the channel walls lead to adhesion when the distances are very close. Authors report that motility is higher in the 10-µm capillary than the 50-µm one [2], and bacteria swim unidirectional in the 6-µm capillary, while the cell speed and run time remain almost the same as the ones measured in the bulk [3]. Biondi *et al.* [4] measured that average cell speeds are the same for channels with 10 µm depths or more, but 10% higher in 3-µm channels and 25% smaller in 2-µm channels than the ones measured in the bulk. Authors state that drag effects are only important for *E.coli* swimming inside channels having a height of 2 µm or smaller, where the channel size is very close to the size of the head. DiLuzio*et al.* [1] performed experiments on smooth-swimming *E. coli* cells, which do not tumble, in rectangular channels having widths (1.3 - 1.5 µm) slightly larger than the diameter of the body of the organism and showed that some types of surfaces are preferred by bacteria than others and wobbling or rotational Brownian motion eventually caused cells to separate from the wall. Authors report that rotational Brownian motion is suppressed more and cells swim faster when cells swim near the porous agar surface than when cells swim near the smooth PDMS surface, and propose that the hydrodynamics is responsible for this behavior. The lower limit for the channel width that *E.coli* and *B.* can continue swimming is discussed by Maennik*et al.* [5]. Authors concluded that *E. coli* can swim in a very close proximity (~40 nm) to a planar surface and adhesive and friction forces exceed the force provided by flagellar motors or bacteria once the diameter of bacterium becomes comparable to the width of the channel [7]. In the same study, authors presented that *E.coli* and *B.subtilus* are still motile in channels having a width approximately 30% larger than bacteria diameters [6].

Near solid boundaries bacteria were observed to follow circular trajectories that are influenced by hydrodynamic effects [4, 5] and altered by Brownian forces that change the distance of the organism from the wall [2, 3]. Vigeant*et al.* [1] studied the attraction between the swimming organisms and a solid surface and proposed that the force holding swimmers near the surface is the result of a hydrodynamic effect when the cells are within about 20 nm to 10 µm of the surface, and electrostatic influences are important when the cells are closer than 20 nm from the surface and lead to the adhesion of the cell. Authors report that stable swimming near the surface for periods well over one minute are observed; ultimately leading cells to move away from the wall by Brownian motion. Lauga*et al.* [7] developed a hydrodynamic model and compared with experiments using *E. coli* bacteria near surfaces and observed that bacteria follow a circular trajectory near a solid boundary as a result of force-free and torque-free swimming and hydrodynamic interactions with the boundary. Authors use the hydrodynamic model to show that the speed and the radius of the circular trajectory of the swimmer depend strongly on the distance to the wall. Li *et al.* [8] report experiments and simulation results for swimming trajectories of singly flagellated bacterium *C. crescentus* near a glass surface. Authors observed that Brownian motion is coupled with hydrodynamic interaction between the bacterium and the surface, influences the swimming of the organism by randomizing the displacement and direction, and leads to the variation of the swimming speed and the trajectory [6]. Experiments performed using *S. marcescens* attached to the 5 µm diameter polystyrene beads showed that beads have helical trajectories away from the wall, however show stochastic behavior near the wall [6].

Hydrodynamic models of low Reynolds number swimming are based on asymptotic solutions of Stokes equations and no-slip boundary conditions, such as presented by Lighthill [7], and resistive force coefficients, that are based on the drag anisotropy on slender rods, e.g. in [8], where present an excellent overview of hydrodynamic models of

swimming. The motion of *E. coli* near a planar surface is modeled using resistive force coefficients and confirmed the resultant circular trajectory with experiments by Lauga*et al.* [9]. Recently, in-channel swimming of infinite helices and filaments that undergo un-dilatory motion is studied by Felderhof [10] with an asymptotic expansion, which is valid for small amplitudes; results show that the speed of an infinitely long helix placed inside a fluid-filled channel is always larger than the free swimmer and depends on the body parameters such as the wavelength, amplitude and the radius of the body.

Analytical models that describe the equation of motion for artificial structures swimming in blood vessels are reported in recent years. Arcese*et al.* [2] developed an analytical model that includes contact forces, weight, van der Waals and Coulomb interactions with the vessel walls and hydrodynamic drag forces on a spherical micro robot in non-Newtonian fluids to address the control of magnetically guided therapeutic micro robots in the cardiovascular system.

In addition to analytical models, there are numerous examples of numerical solutions of Stokes equations for micro swimmers in unbounded media and near planar walls with no-slip boundary conditions; representative ones are the following. Motion of *Vibrio alginolyticus* was modeled numerically by Goto*et al.* [5] with the boundary element method (BEM); authors showed that model results agree well with observations on the strains of the organism that exhibit geometric variations. Ramia*et al.* used a numerical model based on BEM and calculated that the micro swimmer's velocity increases by only %10 when swimming near a planar wall, despite the increase in drag coefficients [4].

No-slip boundary conditions are commonly adopted for modeling microorganisms swimming in unbounded media and near planar walls, e.g. [1-10]. For example, Shum *et al.* used a boundary element method (BEM) to study entrapment of bacteria near solid surfaces, and used no-slip boundary conditions to study swimming of a micron-sized microorganism as near as 35 nm to a planar surface [7]. However, from a general perspective no-slip boundary conditions are questionable especially in sub-micron scales [8]. In addition to molecular forces, wetting and shear rate, slip length in solid-fluid interfaces depends on surface roughness, Nano bubbles, contamination and viscous heating [8]. Although in some studies it is reported that slip exists both on hydrophilic and hydrophobic surfaces and the degree of slip differs according to the wetting of the surface [7], with improvements on the contact angle measurement techniques, boundary conditions on the hydrophilic surfaces are adopted as no-slip by several authors [8]; non zero slip length is observed in the presence of Nano bubbles and at very high shear rates [8]. Blood vessels and other conduits in the human body are covered with hydrophilic surface tissue, which is the endothelium and used to render polymers hydrophilic [8]. In addition, most of the bacteria show hydrophilic surface properties [8]. Therefore, no-slip boundary conditions are assumed for swimming of bacteria in modeling studies, e.g. [8], and adopted here as well.

Another question is about the Newtonian fluids used in experiments and modeling studies. The red blood cells, which present in the blood, cause it to behave like a non-Newtonian fluid [1]. The blood plasma, on the other hand, is a Newtonian fluid and more than 50% of it is water. A micro swimmer would experience the same effects with particles (cells) in the blood, therefore, at the micro and nano scales, blood can be considered as Newtonian fluid for modeling studies [3]. In addition, the experimental results of Liu *et al.* [2], who studied visco-elastic effect of the non-Newtonian fluid using Boger fluid in their scaled-up setup, which is used to measure the force-free swimming speed of a rotating rigid helix, show that the difference in the forward velocities of rotating helices in viscous and visco-elastic fluids is not crucial.

Inspired by microorganisms with helical flagella, swimming of one-link helical magnetic micro structures is demonstrated using external rotating magnetic fields, since artificial reproduction of the mechanism used by natural micro swimmers is very difficult in Nano and micro scales [8]. However, technological challenge may not be too prohibitive in mm-scale, which is still in the low Reynolds number regime. Moreover, swimming of natural microorganisms and magnetically controlled bio-carriers [12] in channels differ than the swimming of one-link artificial swimmers. Thus, experiments with scaled-up robots swimming in viscous fluids have been used to demonstrate the efficacy of the actuation mechanism as well as validate hydrodynamic models, since low Reynolds number flows are governed by Stokes equations regardless of the length scale.

The Reynolds number, which characterizes the relative strength of inertial forces with respect to viscous ones, is given by: $\mathrm{Re} = \frac{\rho U \ell}{\mu}$ where ρ and μ are density and the viscosity of the fluid, and U and ℓ are the velocity and length scales of the flow. According to Purcell [13], a man would experience the same forces and effects as a bacterium if he tries to swim in a pool that is full of molasses; since both situations would have the same low Reynolds number and same physical conditions. For example, the Reynolds number for the swimming of a

generic bacterium with a length scale of 1 µm at the speed of 10 µm/s in water is about, $Re = \rho U\ell/\mu = 1000\times10^{-5}\times10^{-6}/10^{-3} = 10^{-5}$. Similarly, for a cm-scale robot swimming with the speed of 1 cm/s in viscous oil with the viscosity 10000 times the viscosity of water and about the same density as water, the Reynolds number is, $Re = \rho U\ell/\mu = 1000\times10^{-2}\times10^{-2}/\ 10^{4} = 10^{-5}$. Therefore, the hydrodynamic properties of the swimming of bacteria in water and the robot in oil are dynamically similar. The test data obtained for the cm-scale model can be applied to µm-scale one; dynamical similarity is commonly practiced in the design of large scale objects such as aircrafts and submarines as well [14].

There are a number of works reported in literature that takes advantage of the hydrodynamic similarity of low Reynolds numbers and uses experiments in viscous fluids at cm-scales to study the swimming of bacteria in micro-scales. Behkam and Sitti [17] calculated the thrust force generated by a rotating helix using scaled-up characterization experiments; the deflection of a very thin (1.6 mm) cantilever beam due to the rotation of helical body in silicon oil-filled tank is measured to calculate the thrust force. Another scaled-up model is presented by Honda *et al.* [15] where rotating magnetic field is used as external actuation to obtain propagation of a cm-long helical swimming robot in a silicon oil-filled cylindrical channel. The linear relationship between the swimming speed of the robot and the excitation frequency is observed by authors and results agreed well with the hydrodynamic model developed by Lighthill [16] based on the slender body theory for microorganisms. Kim *et al.* [4] analyzed digital video images of a macroscopic scale model that demonstrated the purely mechanical phenomenon of bacterial flagella bundling; the macroscopic scale model allows to determine the effects of parameters that are difficult to study in micro-scale such as the rate, effects of the helical radius and the pitch, which are hard to measure accurately, and the direction of motor rotation [19]. Another study conducted by Kim *et al.* [18] performed to measure the velocity field for rotating rigid and flexible helices, and study the flagellar bundling of *E. coli* or other bacteria, by building a scaled-up model, which ensures Reynolds number to be low, using macro-scale particle image velocimetry (PIV) system.

In our recent experiments, one-link micro robots were placed inside glycerol-filled glass channels of 1 mm inner-diameter and actuated by external rotating magnetic fields [2]. Results of the experiments indicate that a proportional relationship between the time-averaged velocity and the rotation frequency exists up to a step-out frequency, after which the robot's rotation is no longer synchronized with the magnetic field, similar to results observed in almost unbounded fluids in the literature [8]. We also reported computational modeling of one-link swimmers with magnetic heads and helical body's swimming inside glycerol-filled glass channels [21]; the computational model predicted the speed of swimmers well and demonstrated that near wall swimming is faster than center swimming, which is faster than unbounded swimming. Furthermore, the model showed that the rotation of the helical body produces a localized flow around the swimmer leading to forces and torques that alter the orientation of the swimmer in the channel [20].

Hydrodynamic effects need to be studied in order to improve understanding of the motion of micro robots inside vessels, arteries and similar conduits inside the body, as well as the motion of microorganisms inside channels and confinements. However, experiments with microorganisms and artificial micro structures pose many challenges such as controlling the geometry of the body and the body which have a strong influence on the speed and efficiency. Therefore, experiments with cm-sized robots are advantageous since geometric parameters can be controlled and low Reynolds number conditions can be satisfied.

In this study, we describe a computational fluid dynamics (CFD) model, which is validated with experiments reported in our earlier work [4], to analyze the effects of the geometric parameters of the body and the radial position of the robot on the speed and efficiency of the cm-size two-link robot swimming inside a circular channel filled with viscous silicone oil, which ensures low Reynolds number swimming conditions as adopted commonly in literature, e.g. [8]. The CFD model is based on the solution of three-dimensional Stokes equations subject to no-slip boundary conditions on the body and the body of the robot and on channel walls, as commonly used in similar studies for microorganisms swimming near solid walls, e.g. [24] and validated by experimental results. Since, it is established by prior research in the literature that hydrodynamic effects are very important for the near wall swimming of natural organisms, e.g. [8], we carried out a number of simulations with the CFD model to study the effects of body design and the radial position on the swimming performance. Moreover, radial position of magnetic robots inside channels can be a control parameter as well [11] with the use of magnetic manipulation techniques that are demonstrated successfully in velocity and position control of magneto tactic bacteria [19] and artificial structures [2].

EXPERIMENTAL SECTION

The two-link robot used in the experiments is untethered and consists of a body and a helical body similarly to microorganisms. The body of the robot is made of a glass tube of outer diameter of 1.6 cm and thickness of 1mm and a plastic cover with outer diameter of 1.8 cm and length of 1 cm. Inside the glass tube, a power source, Li-polymer battery (3.7 V, 65 mAh) of dimensions 17.3×13.5×13.5 mm^3; a brushless DC motor of diameter of 6 mm and length of 14 mm with 3V DC nominal voltage and 200 mA nominal current; and a small switch of dimensions 7×3×3 mm^3 are held together with an adhesive putty that ensures rotational symmetry and neutral buoyancy of the body. Table 1 summarizes common dimensions of robots.

In order to study the effects of the helical pitch (wavelength) and radius (amplitude) of the helical body on the swimming speed, 15 different helical bodys are made of steel wire of diameter 1 mm. Bodys are manufactured manually by wrapping the steel wire around rigid bars of desired diameter to obtain amplitudes, *B*, of 1, 2, 3 and 4 mm, which corresponds to a ratio between amplitudes and channel diameter, B/R_{ch}, 1/18 (0.056), 2/18 (0.112), 3/18 (0.167) and 4/18 (0.223). Then the coil is plastically deformed by extending it to desired wavelengths that correspond to 2, 3, 4 and 6 turns, N_λ, on the helical body, which has a fixed length, 6 cm; the total length of the wire varies with the wavelength and amplitude. Only the body with the largest amplitude, 4 mm, and the smallest number of turns, 2, was not manufactured with a satisfactory helical shape, thus experiments are not performed with that body. Fixed plastic couplings are used to secure each body to the shaft of the dc-motor that protrudes from the capsule. The robot consisting of the capsule and the body is placed inside an open-ended circular glass channel with the diameter of 3.6 cm and length of 30 cm inside an aquarium filled with silicone oil with a viscosity of 5.6 Pa-s (5000 times the viscosity of water) and a density of 1000 kg/m^3 as shown in Fig. 1c. The body, which is used for all robots, is neutrally buoyant; however robots rest at the bottom of the horizontally placed channels due to the weight of the steel wire body.

Table 1.Common Dimensional Properties for Robots

Radius of the body, r_b	0.8 cm
Total length of the body, L_b	4 cm
Outer radius of the cap, r_{cap}	0.9 cm
Length of the cap, L_{cap}	1 cm
Apparent length of bodys, L_{body}	6 cm
Length of couplings	1 cm
Diameter of body wire, $2r_{body}$	1 mm
Length of the channel, L_{ch}	30 cm
Diameter of the channel, $2R_{ch}$	3.6 cm

Maximum Reynolds number for the robots used in the experiments is calculated using diameter of the capsule body and maximum forward velocity reached by R10 in experiments as length and velocity scales as: $Re = \rho U\ell/\mu = 1000\times(1.01\times10^{-3})\times(16\times10^{-3})/5.6 = 2.89\times10^{-3}$, which is much less than unity confirming that the flow is well within the Stokes regime. As an example, a micro robot with the diameter of 32 µm and velocity of 100 µm/s traveling in water has the same Reynolds number as R10.

For each experiment, the battery that supplies power for the dc-motor is charged fully, the switch is turned on manually and the robot is placed inside the channel near the mid-axis. The motion of the robot is recorded with a CCD camera. Frequencies of body and body rotations and forward velocity of the robot are calculated from orientations of the body and the body, and from the position of the robot in recorded images.

The formulation here is based on that a propeller blade is represented by a lifting line, with trailing vorticity aligned to the local flow velocity (i.e. the vector sum of free-stream plus induced velocity).the total resultant inflow velocity magnitude is composed of inflow velocities, V and induced velocities, u as :

$v = \sqrt{(v_a + u_a^*)^2 + (\omega r + v_t + u_t^*)^2}$ which is oriented at pitch angle, $\beta_i = \arctan(\frac{v_a + u_a^*}{\omega r + v_t + u_t^*})$. Assuming the Z blades are identical, the total thrust and torque on the propeller are

$$T = z\int_{r_h}^{R}[F_i\cos\beta_i - F_v\sin\beta_i]dr(e_a)$$

$$Q = z\int_{r_h}^{R}[F_i\sin\beta_i + F_v\cos\beta_i]rdr(-e_a)$$

where Fi and Fv are the magnitudes of the inviscid and viscous force per unit radius and r_h and R are the radius of the hub and blade tip, respectively. The power consumed by the propeller is $P = Q\omega$ and the efficiency of the propeller is $\eta = \frac{TV}{Q\omega}$ .A standard vortex lattice formulation is used to compute the axial and tangential induced velocities. a radial lifting line, partitioned into M panels. A horseshoe vortex filament with circulation (i) surrounds the ith panel, consisting of helical trailing vortex filaments shed from the panel endpoints (rv(i) and rv(i+1)) and the segment of the lifting line that spans the panel. The induced velocities are computed at control points on the lifting line at radial locations rc(m), m = 1:M, by summing the axial and tangential velocity induced by each horseshoe vortexat rc(m) by a unit-strength horseshoe vortex surrounding panel i.

$$u_a^*(m) = \sum_{i=1}^{M} \Gamma(i) u_a^*(m,i)$$

$$u_t^*(m) = \sum_{i=1}^{M} \Gamma(i) u_t^*(m,t)$$

Since the lifting line itself does not contribute to the induced velocity,

$$u_a^*(m,t) = u_a(m,i+1) - u_a(m,i)$$

$$u_t^*(m,t) = u_t(m,i+1) - u_t(m,i)$$

where $u_a(m;i)$ and $u_t(m;i)$ are the axial and tangential velocities induced at rc(m) by a unit-strength constant-pitch constant-radius helical vortex shed from rv(i), with the circulation vector directed downstream (i.e. away from the lifting line) by right-hand rule. For rc(m) <rv(i):

$$u_a(m,i) = \frac{Z}{4\pi r_c}(y - 2Zyy_0F_1)$$

$$u_t(m,i) = \frac{z^2}{2\pi r_c}(y_0F_1)$$

For rc(m) >rv(i):

$$u_a(m,i) = -\frac{Z^2}{2\pi r_c}(yy_0F_2)$$

$$u_t(m,i) = \frac{z}{4\pi r_c}(1 + 2Zy_0F_2)$$

where

$$F_1 \approx \frac{-1}{2zy_0}\left(\frac{1+y_0^2}{1+y^2}\right)^{\frac{1}{4}}\left\{\frac{u}{1-u} + \frac{1}{24Z}\left[\frac{9y_0^2+2}{(1+y_0^2)^{1.5}} + \frac{3y^2-2}{(1+y^2)^{1.5}}\right]\ln\left|1+\frac{U}{1-U}\right|\right\}$$

$$F_2 \approx \frac{-1}{2zy_0}\left(\frac{1+y_0^2}{1+y^2}\right)^{\frac{1}{4}}\left\{\frac{u}{1-u} + \frac{1}{24Z}\left[\frac{9y_0^2+2}{(1+y_0^2)^{1.5}} + \frac{3y^2-2}{(1+y^2)^{1.5}}\right]\ln\left|1+\frac{U}{U-1}\right|\right\}$$

$$U = \left(\frac{y_0(\sqrt{1+y^2}-1)}{y(\sqrt{1+y_0^2}-1)} \exp(\sqrt{1+y^2}-\sqrt{1+y_0^2}) \right)^z$$

$$y = \frac{r_c}{r_v \tan\beta_\omega}$$

$$y_0 = \frac{1}{\tan\beta_\omega}$$

A hub of radius rh is modeled as an image vortex lattice. The image trailing vortex filaments have equal and opposite strength as the real trailing vortex filaments; they are stationed at radii

$$r_{im} = \frac{r_h^2}{r_v}$$

$$\tan\left[\beta_i^{im}\right] = \frac{r_v(1).\tan\left[\beta_i^{\gamma}(1)\right]}{r_{im}}$$

and the drag due to the hub vortex is

$$D_h = \frac{pz^2}{16\pi}\left[\ln\left(\frac{r_h}{r_0}\right)+3\right]\left[\Gamma(1)\right]^2(-e_a)$$

.In addition, a duct endowed with circulation will induce axial velocity at the lifting line

$$u_{a,d}^*(m) = \sum_{n=1}^{Nd} \Gamma_{d(n)u_{a,d}(m,n)}$$

where$u_{a;d}(m;n)$ is the axial velocity induced at at (x = 0, rc(m)) by a unit-strength vortex ring atx = $x_d(n)$,

$$u_{a,d}^*(m) = \Gamma_d.u_{a,d(m)}^*$$

to include the flow induced by the duct circulation

$$u_{a,d}^*(m) = \sum_{n=1}^{Nd} \Gamma_{(i)u_a^*(m,n)} + \Gamma_d.u_{a,d(m)}^*$$

$$u_t^*(m) = \sum_{n=1}^{Nd} \Gamma_{(i)u_t^*(m,n)}$$

The thrust produced by the duct can be computed in terms of the axial and radial circumferential mean velocities induced on the duct by the propeller, as follows

$$T_d = 2\pi rd.\sum_{n=1}^{Nd}(\rho\left[-u_r^d(n)\right]\Gamma_d\Gamma_{d(n)} - \frac{1}{2}\rho\left[V_a^d+u_a^d(n)\right]^2 C_{D,d\frac{cd}{Nd}})$$

The propeller optimization problem is to find the set of M circulations of the vortex lattice panels that produce the least torque

$$Q = \rho Z\sum_{m=1}^{M}\left\{\left[V_a+u_a^*\right]\Gamma+\frac{1}{2}V^*C_{DC}\left[\omega r_c+V_t+u_t^*\right]\right\}r_c\Delta r_v$$

for a specified thrust, T_s,

$$T = \rho Z\sum_{m=1}^{M}\left\{\Gamma\left[\omega r_c+V_t+u_t^*\right]+\frac{1}{2}V^*C_{DC}\left[V_a+u_a^*\right]\right\}r_c\Delta r_v$$

$$-Hflag.\frac{\rho z^2}{16\pi}\left[\ln\left(\frac{r_h}{r_0}\right)+3\right]\left[\Gamma(1)^2\right]=T_s$$

Where H_{flag} is set to 1 to model a hub or 0 for no hub. In the case of a duct-propeller optimization, the propeller only provides a portion of the total required thrust, Tr. The thrust ratio is defined as

$$\tau = \frac{T_s}{T_r} = \frac{propeller..thrust}{total..thrust}$$

such that the thrust required of the duct is Td = Ts-Tr and the total thrust is Tr = Ts + Td. Inthe case of no duct, Td = 0, and Ts = Tr.To solve this optimization problem by the method of the Lagrange multiplier from vibrational calculus; if T = Ts, the na minimum H coincides with a minimum Q. To find this minimum, the derivatives with respect to the unknowns are set to zero

$$\frac{\partial H}{\partial \Gamma_{(i)}} = 0 \qquad \text{For } i=1\ldots M$$

$$\frac{\partial H}{\partial \lambda_1} = 0$$

Ifa maximum allowable lift coefficient is chosen, (typically, 0:1 <C_{Lmax}< 0:5), then the “optimum" chord is

$$\hat{c} = \frac{\Gamma}{\frac{1}{2}(V^*)C_{L\max}}$$

If the Expanded area ratio, $EAR = Z\int_{rh}^{R} c(r)dr$, is given, then the chord length distribution is scaled as follows

$c(r) = \hat{c}(r)\frac{EAR_{spec}}{EAR}$. To evaluate the required partial derivatives

$$\frac{\partial \Gamma(m)}{\partial \Gamma(i)} = \begin{cases} 0 & (m \neq i) \\ 1 & (m = i) \end{cases} \quad , \frac{\partial \lambda_1}{\partial \lambda_1} = 1$$

$$, \frac{\partial u_a^*(m)}{\partial \Gamma(i)} = u_a^*(m,i) \qquad \frac{\partial u_t^*(m)}{\partial \Gamma(i)} = u_t^*(m,t)$$

$$\frac{\partial V_{(m)}^*}{\partial \Gamma(i)} = \tfrac{1}{2}(V^*)^{-1}\begin{pmatrix} 2(V_a + u_a^* \frac{\partial u_a^*(m)}{\partial \Gamma(i)} + \\ 2(\omega rc + Vt + u_t^*)\frac{\partial u_t^*(m)}{\partial \Gamma(i)} \end{pmatrix}$$

$$= \sin(\beta i(m))u_a^*(m,i) + \cos(\beta i(m))u_t^*(m,i)$$

All other partial derivatives are zero or are ignored.During each solution iteration flow parameters are frozen in order to linearize. The linear system of equations, with the linearized unknowns is as follows

$$\frac{\partial H}{\partial \Gamma} = \rho Z \sum_{m=1}^{M} \Gamma(m).\left[u_a^*(m,i)r_c(m)\Delta r_v(m) + u_t^*(i,m)r_c(i)\Delta r_v(i)\right] + \rho Z V_a(i)r_c(i)\Delta r_v(i)$$

$$+\rho Z \sum_{m=1}^{M} \tfrac{1}{2}C_D \frac{\partial V^*(m)}{\partial \Gamma(i)} c(m)\left[\omega r_c(m) + Vt(m) + u_t^*(m)\right] r_c(m)\Delta r_v(m)$$

$$+\rho Z \sum_{m=1}^{M} \tfrac{1}{2}CDV^*(m)c(m)\left[u_t^*(m,t)\right] r_c(m)\Delta r_v(m)$$

$$+\rho Z \lambda_1 \sum_{m=1}^{M} \Gamma(m).\left[u_t^*(m,i)\Delta r_v(m) + u_t^*(i,m)\Delta r_v(i)\right]$$

$$+\rho Z \lambda\left[\omega r_c(i) + V_t(i)\right]\Delta r_v(i)$$

$$-\rho Z \lambda_1 \sum_{m=1}^{M} \tfrac{1}{2}C_D \frac{\partial V^*(m)}{\partial \Gamma(i)} c(m)\left[V_a(m) + u_a^*(m)\right]\Delta r_v$$

$$-\rho Z \lambda_1 \sum_{m=1}^{M} \tfrac{1}{2}C_D V^*(m)c(m)\left[u_a^*(m,i)\right]\Delta r_v$$

$$-Hflag.\frac{\partial \Gamma_{(1)}}{\partial \Gamma_{(1)}}.\lambda_1 \frac{\rho Z^2}{8\pi}\left[\ln\left(\frac{rh}{r_0}\right) + 3\right]\Gamma(1)$$

$$= 0 \qquad for \qquad i = ...M$$

$$\frac{\partial H}{\partial \lambda_1} = \rho Z \sum_{m=1}^{M} \Gamma(m).\left[\omega r_c(m) + V_t(m) + u_t^*(m)\right]\Delta r_v(m)$$

$$- \rho Z \sum_{m=1}^{M} \tfrac{1}{2} C_D V^*(m) c(m)\left[V_a(m) + u_a^*(m)\right]\Delta r_v(m)$$

$$- Hflag.\frac{\rho Z^2}{16\pi}\left[\ln\left(\frac{rh}{r_0}\right) + 3\right]\Gamma_{(1)}.\Gamma_{(1)} - T_s = 0$$

Once the design operating state of the propeller/turbine is known, the geometry can be determined to give such performance. The 3D geometry is built from given 2D section profiles that are scaled and rotated according to the design lift coefficient, chord length, and inflow angle

$$\{C_L, f_0, f, \alpha I\} = \frac{C_{L0}}{C_{L_I}}.\left\{C_L, f_0, f, \alpha_I\right\}$$

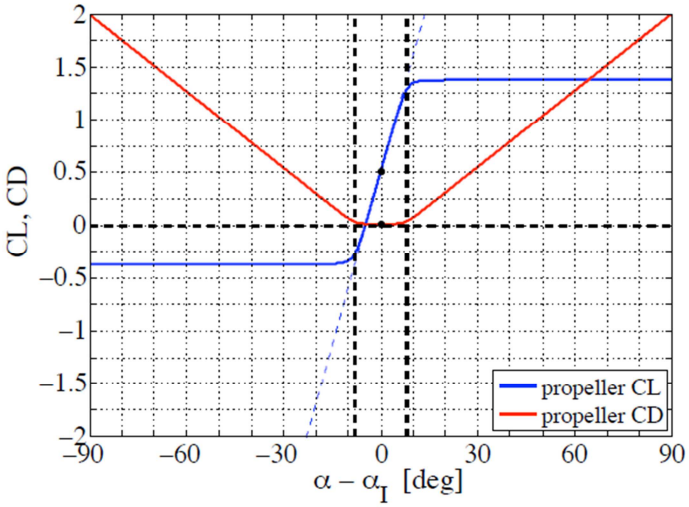

Fig. 4. Lift coefficient, CL, and drag coefficient, CD, versus net angle of attackfor thepropeller

The pitch angle of the blade section is then fixed at

$$\theta = \alpha_I + \beta_{i0}$$

If the analysis of a propeller operating at an off-design (OD) advance coefficient, $J_{s,OD} = \frac{V_s}{n_{OD}D} = \frac{\pi V_s}{\omega_{OD}R}$, the pitch angleof eachblade section is fixed, so the net angle of attack is $\alpha - \alpha_I = \beta_{io} - \beta_i$. The circulation is computed from the 2D lift coefficient, which is given in terms of the loading by

$$C_L = \frac{2\Gamma}{V^* c}$$

The 2D sections lift and drag coefficients given in closed form by equations

$$C_L = C_{L,o} + \tfrac{dc_L}{d\alpha}\Delta\alpha$$

$$- \tfrac{dC_L}{d\alpha}(\Delta\alpha - \Delta\alpha_{stall}).F(\Delta\alpha - \Delta\alpha_{stall})$$

$$+ \tfrac{dC_L}{d\alpha}(-\Delta\alpha - \Delta\alpha_{stall}).F(-\Delta\alpha - \Delta\alpha_{stall})$$

$$C_D = C_{D,0}$$

$$+ A.(\Delta\alpha - \Delta\alpha_{stall}).F(\Delta\alpha - \Delta\alpha_{stall})$$

$$+ A.(-\Delta\alpha - \Delta\alpha_{stall}).F(-\Delta\alpha - \Delta\alpha_{stall})$$

$$- 2A.(-\Delta\alpha_{stall}).F(-\Delta\alpha_{stall})$$

where the auxiliary function F(x) has limits 0 and 1.Each vortex panel state vector, xm, is updated using a Newton solver. Define the residual vector for the m_{th} panel as

$$R_m = \begin{vmatrix} V^* - \sqrt{(V_a + u_a^*)^2 + (\omega OD r_c + V_t + u_t^*)^2} \\ \alpha - (\alpha I + \beta_{io} - \beta_i) \\ C_L - C_L(\alpha) \\ \Gamma - (\frac{1}{2} C_L V^* c) \\ u_a^* - \left([u_a^*][\Gamma] + \Gamma_d u_{a.d}^* \right) \\ u_t^* - \left([u_a^*][\Gamma] \right) \end{vmatrix}$$

In order to drive the residuals to zero, the desired changein the state vector, dx_m, is found by solving the matrix equation

$$0 = R_m + J_m . dX_m$$

where non-zero the elements of the Jacobian matrix are

$$J_m(i,i) = \frac{\partial R_{V^*}}{\partial V^*} = \frac{\partial R_\alpha}{\partial \alpha} = \frac{\partial R_{C_L}}{\partial C_L} = \frac{\partial R_\Gamma}{\partial \Gamma} = \frac{\partial R_{u_a^*}}{\partial u_a^*} = \frac{\partial R_{u_a^*}}{\partial u_a^*} = 1$$

$$J_m(1,5) = \frac{\partial R_{V^*}}{\partial u_a^*} = -\frac{V_a + u_a^*}{\sqrt{(V_a + u_a^*)^2 + (\omega_{OD} r_c + V_t + u_t^*)^2}}$$

$$J_m(1,6) = \frac{\partial R_{V^*}}{\partial u_t^*} = -\frac{\omega_{OD} r_c + V_t + u_t^*}{\sqrt{(V_a + u_a^*)^2 + (\omega_{OD} r_c + V_t + u_t^*)^2}}$$

$$J_m(2,5) = \frac{\partial R_\alpha}{\partial u_a^*} = \frac{\partial R_\alpha}{\partial \beta_i} \cdot \frac{\partial \beta_i}{\partial \tan(\beta_i)} \cdot \frac{\partial \tan \partial \beta_i}{\partial u_a^*} = \frac{1}{1 + \partial \tan^2(\beta_i)} \cdot \frac{1}{\omega_{OD} r_c + V_t + u_t^*}$$

$$J_m(2,6) = \frac{\partial R_\alpha}{\partial u_t^*} = \frac{\partial R_\alpha}{\partial \beta_i} \cdot \frac{\partial \beta_i}{\partial \tan(\beta_i)} \cdot \frac{\partial \tan \partial \beta_i}{\partial u_t^*} = \frac{1}{1 + \partial \tan^2(\beta_i)} \cdot \frac{-\tan(\beta_i)}{\omega_{OD} r_c + V_t + u_t^*}$$

$$J_m(3,2) = \frac{\partial R_{C_L}}{\partial \alpha} = -\frac{dC_L(\alpha)}{d\alpha}$$

$$J_m(4,1) = \frac{\partial R_\Gamma}{\partial V^*} = -\frac{1}{2} C_L c$$

$$J_m(4,3) = \frac{\partial R_\Gamma}{\partial C_L} = -\frac{1}{2} V^* c$$

$$J_m(5,4) = \frac{\partial R_{u_t^*}}{\partial \Gamma} = -u_a^*(m,m)$$

$$J_m(6,4) = \frac{\partial R_{u_a^*}}{\partial \alpha} = -u_t^*(m,m)$$

$$J_m(5,2) = \frac{\partial R_{u_a^*}}{\partial \alpha} = \frac{\partial R_{u_a^*}}{\partial \beta_i} \cdot \frac{\partial \beta_i}{\partial \alpha} = \sum_{j=1}^{M} \Gamma(j) \frac{\partial u_a^*(m,j)}{\partial \beta_i(m)}$$

$$J_m(6,2) = \frac{\partial R_{u_t^*}}{\partial \alpha} = \frac{\partial R_{u_t^*}}{\partial \beta_i} \cdot \frac{\partial \beta_i}{\partial \alpha} = \sum_{j=1}^{M} \Gamma(j) \frac{\partial u_t^*(m,j)}{\partial \beta_i(m)}$$

All other terms are zero or are ignored. The total inflow speed at the duct quarter chord is

$$V^* = \sqrt{(V_a^d + u_a^d)^2 + (u_r^d)^2}$$

The inflow angle at the quarter chord is

$$\beta_i = \arctan\left(\frac{-u_r^d}{V_a^d + u_a^d} \right)$$

The 2D lift coefficient (i.e. lift per unit circumference) for the duct becomes

$$C_{L.d} = \frac{dC_L}{d\alpha} . (\beta_{io} - \beta_i) + C_{L,do}$$

andthe duct circulation then is

$\Gamma_d = \frac{1}{2} V^*_{cd} C_{L,d}$

Table 2. Design Parameters

Variable	Formula	*Description*
V_S	V_s	*shipspeed* (*free* – *streamspee d*)$[m/s]$
R	R	*propeller .radius*$[m]$
D	D	*propeller .diameter*$[m]$
n	n	*rotation .rate*$[rev/s](\omega = 2\pi n)$
Rhub_oR	$r_{h/}R$	*normalized hub radius*
RC	$r_{c/}R$	*normalized control po*int *radius*
DR	$\Delta r_{v/}R$	*normalized difference in.vortex.radii*
CoD	c/D	*normalized* sec*tion chord*
VAC	V_a/V_s	*normalized axial* inf *low velocity*
VTC	Vt/V_s	*normalized* tan *gential* inf *low velocity*
UASTAR	u_a^*/V_s	*normalized induced axial velocity*
UTSTAR	u_t^*/V_s	*normalized induced* tan *gential velocity*
UAHIF	$2\pi R.u_a^*$	*normalized axial horseshoe* inf *luence function*
UTHIF	$2\pi R.u_t^*$	*normalized* tan *gential horseshoe* inf *luence function*
G	$\Gamma/(2\pi R V_s)$	*normalized circulation*
VSTAR	V^*/V_s	*normalized total* inf *low speed*
dVdG	$2\pi R.\frac{\partial V^*}{\partial \Gamma}$	*normalized* $\frac{\partial V^*}{\partial \Gamma}$
dVdW	$\frac{\partial V^*}{\partial \omega}/R$	*normalized* $\frac{\partial V^*}{\partial \omega}$
LM	λ_1/R	*normalized langrange multiplier*
CT	$C_T = \frac{T}{\frac{1}{2}\rho V_s^2 \pi R^2}$	*thrust coefficient based on ship speed*
CQ	$C_Q = \frac{Q}{\frac{1}{2}\rho V_s^2 \pi R^3}$	*torque coefficient based on ship speed*
CP	$Cp = \frac{Q\omega}{\frac{1}{2}\rho V_s^3 (\pi R^2)}$	*power conefficient*$(Cp = \frac{\omega R}{V_s} C_Q = \lambda C_Q = \frac{cQ\pi}{J_s})$
KT	$K_T = \frac{T}{\rho n^2 D^4}$	*thrust coefficient based on blade tip speed*
KQ	$K_Q = \frac{Q}{\rho n^2 D^5}$	*torque coefficient based on blade tip speed*
J_S	$J_S = \frac{V_S}{n\ D} = \frac{\pi V_S}{\omega R}$	*advance coefficient*
L	$\lambda = \frac{\omega R}{V_s} = \frac{\pi}{J_S}$	*tip – speed ratio*

RESULTS AND DISCUSSION

In order to analyze hydrodynamic effects of geometric parameters of the body and the radial position of the robot on the swimming velocity, forces, torques and the efficiency of the robot, a CFD model is developed and validated with the experimental results. Simulations are performed for the same geometric parameters of the robot and the channel as the ones used in the experiments, and for radial positions varying between 0 and 8.9 mm, which corresponds to the case when the robot is only 0.1 mm away from the channel wall.

Body of the robot is modeled almost identically as the body used in the experiments with the union of a sphere and a cylinder (see Figs. 1a and 2). As a connector between the body and the helical body, another cylindrical piece is attached to the bottom of the body; finally a helix is used to model the body. Dimensions of the robots modeled here are the same as the robots used in the experiments.

In this paper, several propellers are designed to give the same thrust coefficient, CT = 0.512 ($\{C_L, f_o, f, \alpha_I\} = \frac{C_{L_0}}{C_{L_I}}.\{C_L, f_o, f, \alpha_I\}$), for a range of design advance coefficient $J = \frac{V_s}{nD} = \frac{\pi V_s}{\omega R}$. Each is a hub-less, five-bladed propeller with a diameter D = 1 mm, hub diameter D_{hub} = 0.2 mm, and speed Vs = 0.001 m/s($C_L = C_{L\max}.\frac{\Gamma}{|\Gamma|}$).The chord lengths are optimized for each propeller, with CL_{max} = 0.2 ($C = \frac{2|\Gamma|}{(V^*)C_{L\max}}$ $C_L = \frac{F_i}{\frac{1}{2}\rho(V^*)^2 c} = \frac{2\Gamma}{(V^*)c}$), and $EFFY = \frac{2}{1+\sqrt{1+C_T}} = 0.8970$. By $K_T = \frac{\pi}{8} C_T . J_s^2$ and $\tan\beta = \frac{V_s}{\omega r} = \frac{J_s}{\pi}.\frac{R}{r}$ then

$$T = Z\int_{rh}^{R}\left[|F_i|\cos\beta_i + F_u \sin\beta_i\right]dr(-e_a)$$

$$= Z\int_{rh}^{R}\left[F_i\cos\beta_i - F_u\sin\beta_i\right]dr(e_a)$$

$$Q = Z\int_{rh}^{R}\left[|F_i|\sin\beta_i - F_u\cos\beta_i\right]rdr(e_a)$$

$$= Z\int_{rh}^{R}\left[F_i\sin\beta_i - F_u\cos\beta_i\right]rdr(-e_a)$$

where By $P = Q\omega$

$$o = \frac{\partial Q}{\partial \Gamma_{(i)}} = \rho Z\sum_{m=1}^{M}\Gamma(m).\begin{pmatrix} u_a^*(m,i)r_c(m)\Delta r_v(m) + \\ u_a^*(i.m)r_c(i)\Delta r_v(i)\end{pmatrix}$$

$$+ \rho Z V_a(i) r_c(i)\Delta r_v(i)$$

In the low Reynolds number creeping flow regime, inertial forces are negligible, and incompressible flow is governed by viscous forces balanced by the pressure gradient subject to continuity:

$$\mu\nabla^2\mathbf{u} - \nabla p = 0 \quad \text{and} \quad \nabla\cdot\mathbf{u}=0$$

Then $u_a^*(m,i) \approx \begin{cases} 0 & (m\neq i) \\ u_a^*(i,i) & (m=i)\end{cases}$ and $u_a^*(i) \approx \Gamma(i)u_a^*(i,i)$ So $0 = \rho Z.\Gamma_{(i)}.\left[2u_a^*(i.i)r_c(i)\Delta r_v(i)\right] + \rho Z.V_a(i).r_c(i)\Delta r_v(i)$ and

$u_a^*(i) = -\frac{1}{2}V_a(i)$ .with $u_t^* \equiv u_{t,ADS}^*$ and $[u_t^*][\Gamma] = [u_{t,ADS}^*]$ then $\lambda OD = \frac{\omega_{OD}R}{V_S} = \frac{\pi}{J_{S,OD}}$

In other word $P_E \equiv R_S V_S$ and $P_D \equiv (2\pi n)Q$ leads to performance of $\eta D \equiv \frac{P_E}{P_D}$. By

$$V_A \equiv \frac{1}{\pi R^2 - \pi R_{hub}^2} \int_{R_{hub}}^{R} 2\pi r V_a(r) dr$$

In addition, $P_T \equiv TV_A$ so $\eta B \equiv \frac{P_T}{P_D} = \frac{TV_A}{(2\pi n)Q} = \frac{J_S}{2\pi} \frac{K_T}{K_Q} \frac{V_A}{V_S}$. Where $\eta_0 \equiv \frac{T_0 V_A}{(2\pi n)Q_0}$, $\eta_R \equiv \frac{\eta_B}{\eta_0}$,

$(1-\omega_v) = \frac{V_A}{V_S}$, $(1-t) = \frac{R_S}{T}$, $\eta_H \equiv \frac{P_E}{P_T} = \frac{R_S V_S}{TV_A} = \frac{(1-t)}{(1\_\omega_v)}$, $\eta_D = \eta_H \eta_B = \eta_H \eta_R \eta_0$, $\eta_S = \frac{P_D}{P_S}$,

$\eta_P = \frac{P_E}{P_S} = \eta_D \eta_S = \eta_H \eta_B \eta_S$, $\{C_T^*, K_T^*, K_Q^*, \eta_B^*, ...\} versus\ J_S^*$.

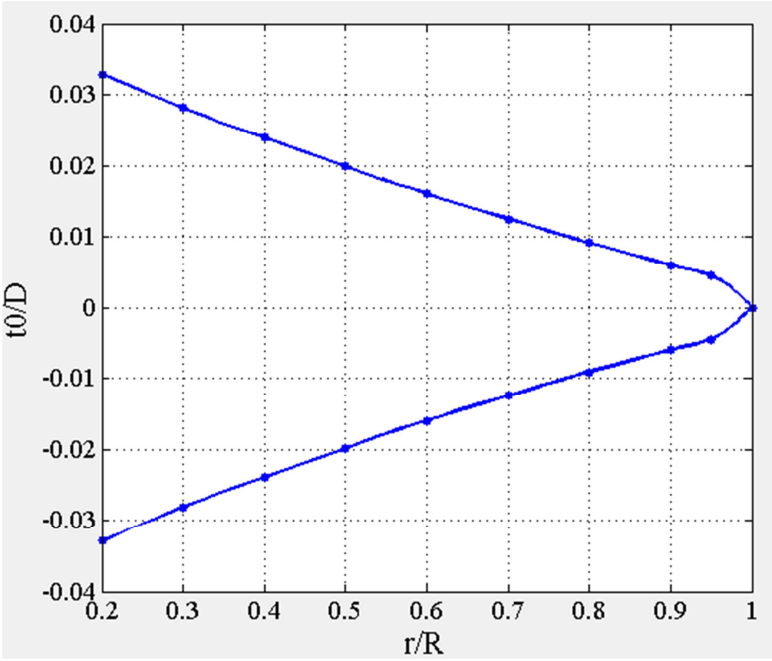

Fig. 5.blade thickness

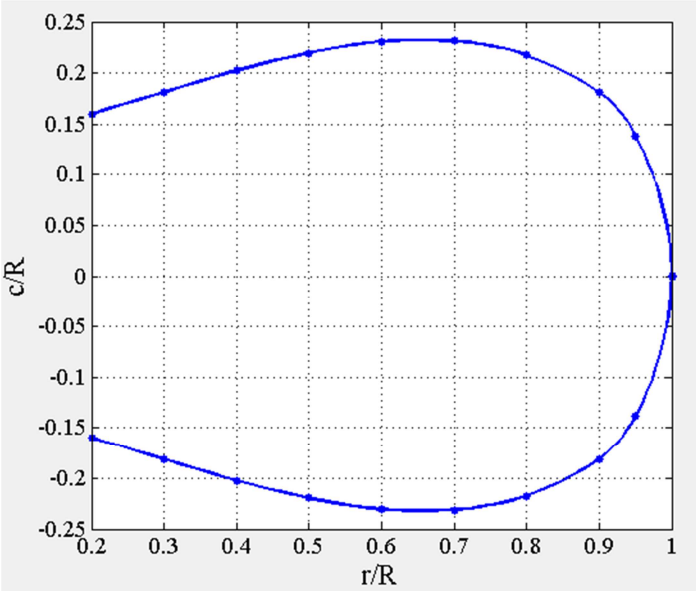

Fig. 6.Dimensional parameters and layout of the robot blade

Since its overall performance is $T = \frac{R_S}{(1-t)}$, $C_T = \frac{T}{\frac{1}{2}\rho V_s^2 \pi R^2}$, $J_s = \text{interpolate}(C_T^*, J_S^*, C_T)$,

$\eta_B = \text{interpolate}(J_S^*, \eta_B^*, J_S)$, $KQ = \text{interpolate}(J_S^*, K_Q^*, J_S)$, $n = \frac{V_S}{J_S D}$, $Q = K_{Q\rho n^2} D^5$, $P_D = (2\pi n)Q$,

$P_S = \frac{P_D}{\eta s}$, $\eta_H = \frac{R_S V_S}{T V_A}$, $\eta_P = \eta_D \eta_S = \eta_H \eta_B \eta_S$ where μ is viscosity, **u** is the velocity vector and *p* is pressure.

Inlet and outlet of the channel are set to open boundary conditions, i.e. the normal stresses are zero:

$(-p\mathbf{I} + \sigma)\mathbf{n} = 0$ at $x = 0, L_{ch}$.

No-slip boundary conditions are adopted here at the channel walls and on the swimmer's surface. The velocity at the channel wall is set to zero:

$\mathbf{u} = 0$ at $r = R_{ch}$

The swimming robot moves with a forward velocity, *U*. Therefore, no-slip moving-wall boundary conditions for the body is specified as:

$\mathbf{u}(\mathbf{x}) = [U, 0, 0] + [0, y, z - r_{sw}] \times [\Omega_b, 0, 0]$ for $\mathbf{x} \in S_{body}$

where$r_{sw}$is the position of the robot in the **z**-direction and varied between 0 (centerline) and a value, which corresponds to a small gap between the body and the channel wall; Ω_b is the body rotation rate; and ω is the rotation rate of the body.

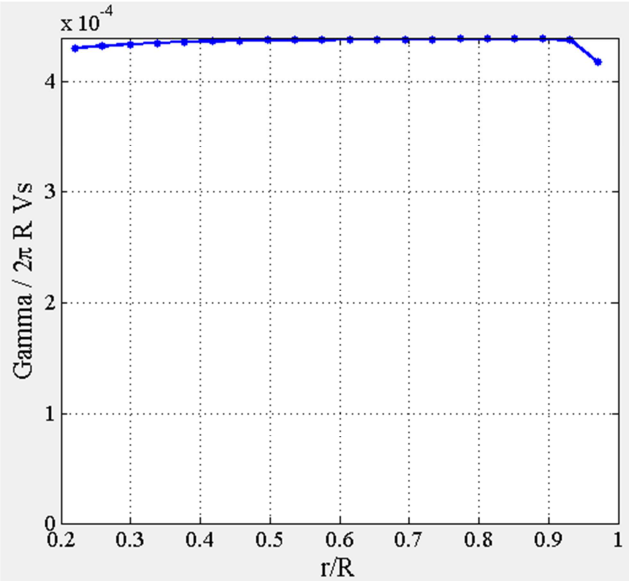

Fig. 7.Circulation of the robot blade

The closest distance between the robot and the channel wall is set to 0.1 mm in simulations. Therefore, no slip boundary conditions apply well for experiments that are conducted in cm-scales. Moreover, according to experiments conducted on natural micro swimmers and reported in literature, e.g. [1], electrostatic influences are important when the cells are closer than 20 nm from the surface. The ratio of the length scales based on the proximity of the robots is 5000, hence, results can be deemed applicable for robots with 3.2 μm in diameter swimming in a channel with diameter of 7.2 μm.

Other external forces, such as gravity, magnetic forces and torques, electrostatic forces and random Brownian effects acting on the swimmer are neglected. Governing equations given subject to constraint equations and boundary conditions are solved with the finite-element method (FEM), commercial Multiphysics software. The finite-element model consists of approximately 90K tetrahedral elements and 450K degrees of freedom. The linear system of equations is solved using the PARDISO direct solver. For each specified position and body design, phase averaged velocities, forces, torques and efficiencies are obtained from the average of 12 angular positions of the body varying between π/6 and 2π. In total, 16×8×12=1536 three-dimensional simulations are performed in addition to mesh convergence studies for selected body's and radial positions. Each simulation takes about 3 to 5 minutes on

a high end workstation with 12 cores operating at 2.7 GHz and sharing 96 GB or RAM. Fig. 2b shows the mesh distribution when the distance between the robot and the channel wall, w_d, equals 0.1 mm with the finest mesh.

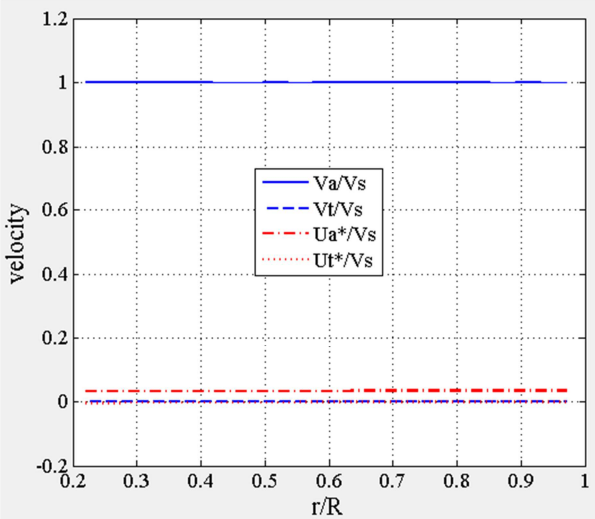

Fig. 8.Induced velocities

In simulations, radial position of each robot in the channel is varied between 0 and 8.9 mm, which is specified only in the **z**-direction with respect to the centerline of the channel for y = 0 (see Fig. 2). For r_{sw}= 0, the axis of the robot lies on the centerline of the channel, and for r_{sw}= 8.9 mm, the closest distance between the body and the channel wall, w_d, is only 0.1 mm. In order to set the position of robot closer than 0.1 mm, restrictive constraints on the finite-element mesh are necessary for accurate solutions. Moreover, as results indicate any further increase in the proximity of the robot to the channel wall does not change the trend in the forward velocity, which should go to zero for the robots that adhere on the wall.

Experiments are performed with fifteen different designs amplitudes to obtain the forward velocity of the robot and the rotation rates of the body. Experimental results are compared with the ones from CFD simulations to validate the CFD model, which is then used to predict the effect of the radial position on the velocity, forces and torques acting on the robot and the efficiency.

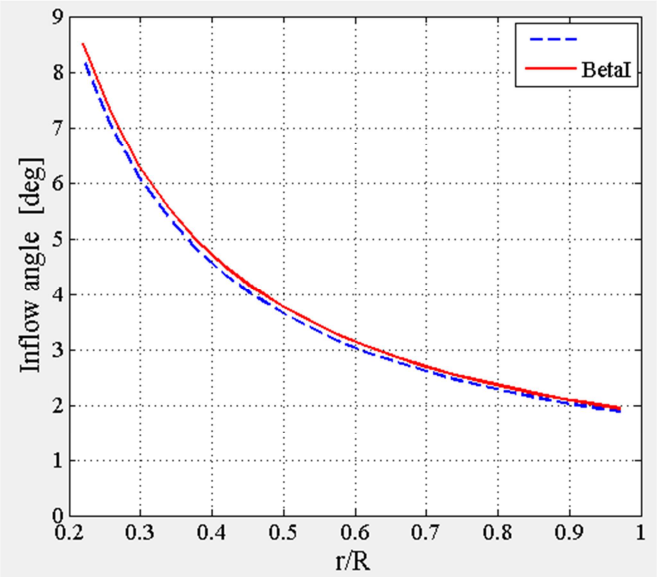

Fig. 10.Inflow angle

Hydrodynamic models and numerical results indicate that the forward velocity increases with the frequency and amplitude, but has an optimum for the wavelength, which depends on other parameters such as the size of the body and the length of the body. In the experiments, the frequency of the body rotation varies according to the torque

balance for each body; therefore theoretical trends are not discernible easily. The rotation frequency of the body decreases with increasing number of waves and the amplitude due increasing viscous torque. Therefore the body's rotation frequency and the forward velocity are at their maximum values for each body according to the current and power constraints of the battery and the dc motor.

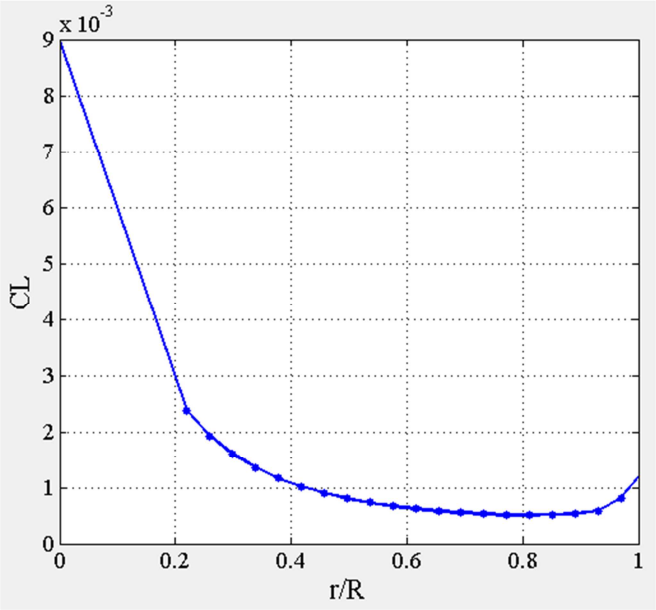

Fig. 11.Lift coefficient

In the experiments, maximum forward velocity is 1.01 mm/s for the robot with a helical body that has 3 full waves, 3-mm amplitude, and rotating with the frequency of 2.49 Hz; the minimum forward velocity is 0.32 mm/s for the robot with 6 full waves and 4mm amplitude, for which the body's rotation frequency is the smallest as well, 0.89 Hz.

The frequency of rotations of body's and bodies vary significantly between robots. Frequency of body rotations is larger for body's with small amplitudes (between 4.3 and 8.2 Hz for B = 1 mm) than bodys with large amplitudes (between 0.9 and 1.2 Hz for B = 4 mm). However, rotational frequency of the body, in principle, is expected to be constant as long as the torque provided by the motor is constant. Variation in body rotation rates could be due to the power-angular velocity relationship of the DC motor, and the varying distance between robots and the channel wall; part of the robot's weight comes from the body and increases with the actual length of the wire, which increases with the amplitude and the number of helical waves. Furthermore, exact radial positions of robots were difficult to measure in the experiments; it is expected that robots travel as close as possible to the channel wall due to the weight of the body. Moreover, the adhesion of the robot on the channel wall is not observed in experiments; for all cases, rotation of the body and the forward motion always prevailed. We used computational fluid dynamics to model the flow and obtain forward velocity and body rotation rate for observed body rotation rates in experiments for each robot to confirm that the motion of robots is dominated by hydrodynamic effects. In the experiments, it is observed that swimming robot travels near the channel wall due to body's weight. In the CFD model, the radial position of the swimming robot is varied, and near wall results are used in the validation of the model.

Experimentally obtained forward velocities are compared with CFD simulation results in Fig. 3. In the experiments, it is observed that swimming robot is moving at the bottom of the channel, but the distance between the channel wall and robots could not be determined.

When the distance between the channel and the robots is 0.1 mm and 0.2 mm, velocity of the robots obtained from simulations agree reasonably well with experimental results, particularly for B = 2 mm, 3 mm, and 4 mm (Fig.3b, Fig.3c, and Fig.3d). When B = 1 mm, simulation results for robots having a distance of 0.2 mm to the channel is in a better agreement than the case for which the distance is 0.1 mm, although the results are very close. Velocities obtained from CFD simulations for the robots travelling near the wall with a clearance of 1 mm are somewhat higher than the velocities obtained in experiments. The velocities are on the order of 1 mm/s, and the fastest robot has 3 full waves on its helical body with the amplitude (radius of the helix) equals to 3 mm (R10 in Fig.3c).

In the case of one-link swimmer with a helical body attached to a permanent magnet reported in [2], forward velocity of the swimmers is larger near the wall than at the center of the channel. Furthermore, although a one-to-one comparison with the one-link magnetic swimmer is not applicable because of differences between ratios of dimensions of heads and body in two cases, the decrease in velocities for B = 4 as N_λ increases is similar for both cases.

Analytical studies show that, swimmers with helical body in unbounded fluids and in cylindrical channels have an optimal value of wavelength that maximizes the swimming speed. Based on an analysis using stoke lets, Higdon [3] presented that for the same rotational speed, the optimum number of waves that maximizes the swimming speed is 3 for a swimmer with L/A and a/A equal 10 and 0.02, respectively, where L is the length of the flagellum, A is the radius of the body and a is the radius of the flagellum. Higdon [12] also stated that the optimum number of waves depends strongly on the geometry of the swimmer and the decrease in the swimming speed for number of waves greater than the optimum value is a result of the decrease in the efficiency, since the helical structures lose their slenderness as wavelength decreases.

Optimal number of waves that maximizes the swimming speed depends on the body geometry as shown in Fig. 3. For B = 2, 3 and 4 mm, optimal numbers of waves are 3, 2 and 1 (last result is according to simulations), respectively.

When B = 1 mm, swimming speed shows a different trend than the rest as rotational frequencies of body and body are smaller for robots R2 and R3 than R1 and R4. Differences in rotation rates can be attributed to variations in the distance between the robot and the channel wall.

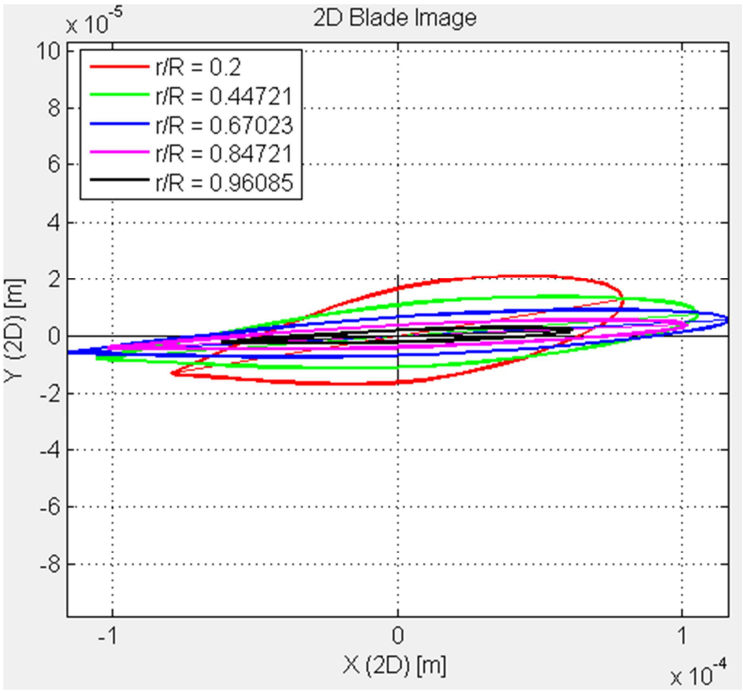

Fig. 12.2D Image of blade

In Fig.4, forward velocities are normalized with the rotational frequency of the body to eliminate the effect of the frequency variations on the forward velocity, so that the effect of the amplitude and the wavelength can be identified. In fact, U/f, represents the stroke, which is the distance traveled for a full rotation of the body. CFD simulations agree very well with experimental results particularly for robots swimming near the channel wall with a distance of 0.1 mm and 0.2 mm especially for B = 2 mm.

According to experiments and near-wall simulations the stroke, U/f, increases with the amplitude. Although the simulation results predict that the U/f increases with N_λ for B = 1 mm, experimental results indicate that there is an optimal value of the number of waves on the body (Fig. 4a). Simulation results agree with the experimentally measured results in predicting that there are optimal values of N_λ for B = 2 and 3 mm (Figs. 4b-c), and that U/f decreases with N_λ for B = 4 mm (Fig. 4d).

The effect of the radial position on the velocity of the robot is shown in Fig. 5, where the radial position of the swimmer, r_{sw}, is normalized with the channel radius, R_{ch}. For all amplitudes and number of waves, the stroke is higher for robots closer to the wall than the ones at the center up to almost 30%; in particular when the normalized radial position, r_{sw}/R_{ch}, is about 0.4. Similarly, 30% increase in the forward velocity is observed for the one-link swimmer as well for r_{sw}/R_{ch} about 0.5 [1]. This improvement in the forward velocity can be attributed to the reduction in the body resistance coefficient near the wall as discussed in Section results.

For radial positions greater than the optimal value that corresponds to the minimum resistance of the body, velocities of robots decrease sharply due to increased shear near the wall; it is plausible that expected velocity of the robot goes to zero when the distance from the wall is below a limit, for which molecular interactions between the robot and the channel wall as observed in experiments with microorganisms [12].

Results also confirm that Brownian forces cause more variations for micro structures and organisms swimming near the wall than the ones far away as reported in [6]. Near the wall small changes in the position cause large variations in the velocity, away from the wall since the velocity is fairly uniform, small changes in the position lead to small variations in the velocity.

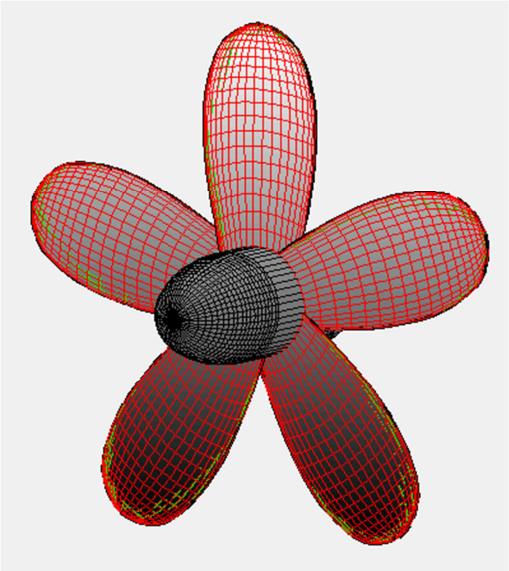

Fig. 13.3D Image of blade

In Fig. 5, it is also observed that the number of waves has a positive effect for B = 1 mm (Fig. 5a), for which the stroke increases with the number of waves for all radial positions; although the increase with the radial position is not as much for N_λ = 2 as other values of N_λ. For B = 2 mm, the stroke is the highest for all radial positions in the case of N_λ = 4, and the lowest for N_λ = 2; strokes are almost identical for N_λ = 3 and 6 at all radial positions (Fig. 5b). For B = 3 mm, strokes are very similar for all number of waves and radial positions; however the increase in the stroke with the radial position is not as pronounced as other values of N_λ than 6 (Fig. 5c). This is also the case for B = 4 mm, for which the stroke for N_λ = 6 is significantly lower than others followed by the stroke for N_λ = 4, which does not increase as much as it does for N_λ = 2 and 3 near the wall (Fig. 5d).

Furthermore, differences between experiments and CFD results in Fig. 4 can be attributed to, in part, the actual radial position of the robot for each body in the experiments. Although the closest distance to the channel wall is set to 0.1 mm in the simulations, the distance of each robot is expected to vary in the experiments. Therefore, one can conclude that robots travel closer to the channel wall for B = 3 and 4 mm, as experimentally measured velocities are smaller than the ones predicted by the CFD model, since robots slow down as they travel closer to the channel wall as shown in Fig. 5. The interpretation presented here, also agrees with the weight of individual body's that increase with the wire length (curvilinear length) of each body, which is given by $\ell = [L^2 + 4\pi^2 B^2 N_\lambda^2]^{1/2}$, where L is the length of the helix. As the weight of the robot increases due to increasing amplitude and number of waves, the average distance between the robot and the channel wall must decrease.

Normalized body rotation rates with respect to angular velocities of body are compared in Fig. 6. Simulation results indicate that the normalized body rotation rate increases with the number of waves and agree very well with experimental results when the distance from the wall, w_d, is between 0.1 and 0.2 mm. Furthermore, for B = 2 mm, simulation results for w_d = 0.2 mm agree much better with experiments than the simulation results for the rest do indicates that R5-7 swim not very close to the wall. Simulation and experimental results show that according to the

geometry of the body, the position of robots changes but distance between robot and channel wall is always below 0.2 mm.

In Fig. 7, the body resistance coefficient, which is the ratio of the axial force on the body to the axial velocity of the robot, $F_{x,body}/U$, is plotted against the radial position for each robot using the results of the CFD model. As the number of waves and the amplitude of the helical body increase, body resistance coefficients stay constant for center-swimming as expected, and indicate that body parameters do not have a significant effect on the body resistance coefficient. However, as the radial position increases, body resistance coefficients decrease to a minimum value where the velocity of the robot almost reaches its maximum (Figs. 5 and 7). As robots get further closer to the channel wall, the body resistance coefficient reaches to the same value as the one at the center of the channel.

For all amplitudes and number of waves, the body resistance coefficient takes a minimum value for the normalized radial position of about 0.4. According to Happel and Brenner , resistance of a small sphere traveling inside a cylindrical channel reaches its minimum value for normalized radial position nearly equals to 0.3 at low Reynolds numbers confirming the advantage of off-center swimming.

Since the force-free swimming condition is applied only in the **x**-direction and the motion of the robot is restricted in other directions, resulting forces acting on the robot along the radial direction (i.e. the negative **z**-direction for y = 0) are presented in Fig. 8 as a function of the radial position. As the number of waves on the helical body and the amplitude increase, there is not a clear indication of a net radial force on the robot for r_{sw}/R_{ch} values between 0 and 0.3. Occasional variations are attributed to lower order of accuracy in the calculation of forces than the accuracy in the calculation of the velocity [17]; force calculations are based on the stress tensor, which uses derivatives of velocity components, which are projected on to second-order polynomials in the finite-element representation. In order to ameliorate the problem finer mesh than the one used in the simulations is necessary; however for the three-dimensional simulations presented here, any further improvement in the finite-element mesh remains too restrictive, and is not critical for the purposes of this work.

Body parameters do not have a significant effect on the radial force. As the robot gets closer to the wall, radial force increases first up to w_d= 0.2 mm, then a sudden fall and change of direction is observed in Fig. 8 for all amplitudes and wavelengths. Very close to the wall, i.e. w_d = 0.1 mm, the **z**-direction force becomes negative, i.e. the radial force is positive, indicating a push towards the wall due to hydrodynamic effects only, when the robot is parallel to the channel's axis. Based on this result and the weight of the robot, adhesion of the robot on the channel walls is expected, but not observed in experiments. The deviation can be attributed to the effect of the orientation of the robot, a pitch angle, or a yaw angle, with respect to the surface, may play an important role in the magnitude and the direction of the radial force when the robot is very close to the wall. The increase in the **z**-direction force is also observed for the one-link magnetic swimmer in [7] but the sudden fall is not observed.

Since the body and the body counter-rotate, lateral forces on each link occur in opposite directions. Net positive **y**-direction (also the tangential direction) force indicates that the rotation of the body dominates the force due to the rotation of the head (Fig. 8e - values are not shown here).

Torques acting on the swimming robot are calculated in CFD simulations and presented in Fig. 9. As the number of waves and the amplitude increase, magnitude of the torque along the **z**-direction also increases between r_{sw}/R_{ch} = 0 and 0.45. As the distance from the wall decreases further, magnitude of the **z**-torque decreases. The difference between the **z**-torque values of robots having different number of waves on the helical body becomes discernible as the amplitude of the helical wave increases (Fig. 9). In all cases, robots having bodys with 6 waves are affected the most from the net negative **z**-torque consistent with experiments (Fig. 9). Lastly, a small positive **y**-direction torque is observed for all cases (not shown here) indicating that the body pushes itself away from the wall (see Fig. 9), leading to a positive pitch angle as suspected in the behavior of the radial force near the wall.

Efficiency of swimming robots is calculated from the ratio of the rate of work done to move the robot in the swimming direction and the rate of work done to rotate the body, as defined by Purcell for low Reynolds number swimmers [14]. The net force on the robot in the direction of its motion is zero, thus only the drag force on the body is considered for the work done in the swimming direction, as also adopted in other studies for the definition of the efficiency of micro swimmers [15]. The net rate of work done by the rotation of the body is calculated from the net angular velocity of the body with respect to the body. Thus, the efficiency of swimming robots is obtained from:

$$\eta = \frac{U \int_{S_{body}} \sigma \cdot \mathbf{n}_x dS}{T_x \left(\omega + \Omega_b\right)}$$

Here U is the forward velocity, σ is the stress tensor, $\mathbf{n}_x$ is the **x**-component of the surface normal, T_x is the rotational torque acting on the body in the **x**-direction, ω is the angular velocity of the body and Ω_b is the angular velocity of the body.

Efficiencies of swimming robots are shown in Fig. 10. For B = 1 mm, the efficiency of the robot increases with the number of waves on the body and varies slightly with respect to the radial position of the robot: it increases with the radial position of the robot up to a maximum around 0.1% for N_λ = 6 near the wall, then decreases with the further increase of the radial position (see Fig. 10).

For B = 2 mm, there is a significant increase in the efficiency of the robot, compared to B = 1 mm, about 0.35% near the wall for N_λ = 3 or N_λ = 4, for which the efficiency is significantly larger than for N_λ = 6 (see Fig. 10). For B = 2 mm, number of waves (helical turns) that leads to the least efficient design is 2. The effect of the radial position on the efficiency is clearly visible: there is an optimal position for robots for about r_{sw}/R_{ch}= 0.44 (i.e. w_d = 1 mm).

For B = 3 and 4 mm (Fig. 10 and 10), efficiencies are larger than for B = 1 and 2 mm; about 0.6% for B = 3 mm and almost 1% for B = 4 mm. For N_λ = 6, efficiency remains almost constant with respect to the amplitude and with the radial position of the robot. For B = 3 mm, most efficient designs have N_λ = 2, 3 and 4 with slight changes in values, and a cross-over between the values at the center and near the wall for N_λ = 2 and 4: the former is slightly more (less) efficient at the center than the latter at the center (near the wall) as shown in Fig. 10.

Although the difference between N_λ = 2 and 3 is still very small, the distinction between the efficiencies of robots with N_λ = 2, 3 and 4 is clearer for B = 4 mm. However, robots with N_λ = 2 is clearly more efficient than for N_λ = 3, 4 and 6 in decreasing order especially near the wall where the efficiency is almost 1% (Fig. 10d). Lastly, the effect of the radial position is very small for the robot with N_λ = 6: the efficiency remains unchanged for all positions except very close to the wall, for which the efficiency exhibits a decline as the radial position increases.

Overall, the pattern indicates that efficiency increases with the wave amplitude (radius) of helical bodys. However, the number of waves has a nonlinear effect: larger number of waves for small amplitudes leads to higher efficiencies, and vice versa. Moreover, the efficiency is consistently larger for robots traveling near the wall than the ones traveling at the center.

CONCLUSION

In this study, experimental and simulation results are presented for cm-scale autonomous swimming robots inside a viscous-fluid filled channel to mimic the swimming of micro robots in aqueous solutions inside blood vessels and other conduits. A computational fluid dynamics (CFD) model is used to solve three-dimensional Stokes equations that govern the flow, and validated with experiments. Forward swimming and body-angular velocities of the robots are measured in experiments and compared with CFD model results for the same robots traveling at radial positions that vary between the center of the channel and 0.1 mm away from the wall in order to understand the effect of the radial position inside the channel. Simulation results for robots swimming near the wall agree very well with experimental results, where the robots swim very near the wall in experiments as well.

Swimming velocity and the efficiency of robots peak at a radial position, which corresponds to 1 mm distance from the wall for all wave amplitudes and number of waves; almost 25% increase in the efficiency is observed for the robot with B = 4 mm and N_λ= 2 and traveling near the wall, compared to the one with the same parameters traveling at the center of the channel. Efficiency of the robots increases with the amplitude; however the effect of the wavelength is nonlinear: small wavelengths have higher efficiency at small amplitudes, or vice versa.

Body resistance coefficients of the robots are calculated in CFD simulations, according to which the resistance coefficients decreases with the radial position of the robots up to almost 25% near the wall, compared to the value at the center. Furthermore, the body parameters, namely the amplitude and wavelength, have a small effect on the body resistance coefficient of the swimming robots, which have significantly larger bodies compared to body.

The radial force on the robot is negligible in the core region of the channel, slightly negative towards the center for the robots closer to the wall before it changes sign and sharply increases when the robot is very close to the wall.

The pull towards the wall can combine with the gravity and increases the proximity of the robot to the channel wall leading to its adhesion; however this is not observed in experiments. There is a slight **y**-torque that indicates the robot may travel with a small pitch angle, which may have an effect on the radial force. It is part of our ongoing efforts to identify the role of orientation of the robot in the channel.

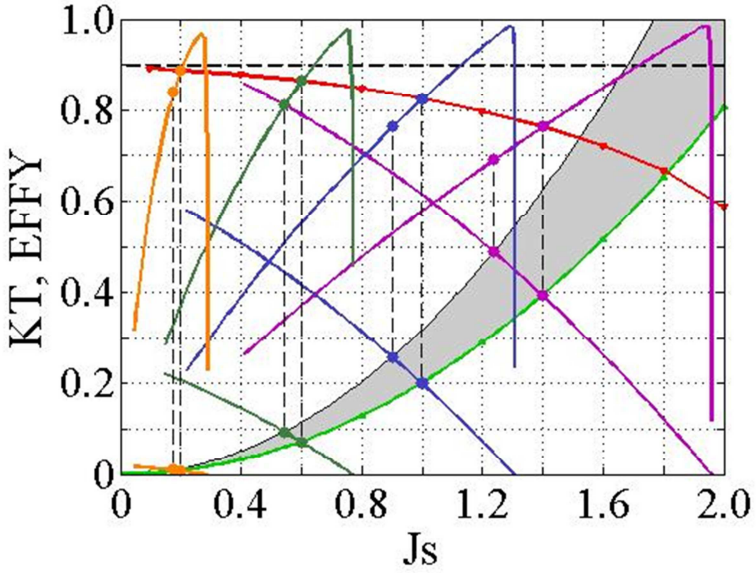

Fig. 14.Performance curve of nanorobot propeller

CONCLUSION

Three-dimensional governing partial differential equations of the fluid flow, Stokes equations, are solved with computational fluid dynamics (CFD) to predict velocities of robots, which are compared with experiments for validation, and to analyze effects of blade number, pitch and the radial position of the robot on its swimming speed, forces acting on the robot and efficiency. Results provide valuable insight for the design of micro robots for in vivo operations inside vessels, arteries and similar body conduits. Swimming velocities of the robots strongly depend on the geometry of the channel as well as amplitude and the wavelength of the body as well as the radial position of the robot.

REFERENCES

[1] MY AbdollahzadehJamalabadi, *J Porous Media*, **2015**, 18(9) ,843-860.
[2] MY AbdollahzadehJamalabadi, *Int J Opt Appl*, **2015**, 5 (5) , 161-167
[3] MY AbdollahzadehJamalabadi, *ChemEng Res Des*, **2015**, 102 , 407-415
[4]MY AbdollahzadehJamalabadi; JH Park ; CY Lee, *entropy*, **2015**, 17 (2), 866-881
[5] E. M. Purcell, **1976**,*Am. J. Phys*, 45 (1), 3-11.
[6] J P Armitage and R M Macnab,**1987**,*J. Bacteriol.*, vol. 169, no. 2, 514-518.
[7] T Atsumi, Y Maekawa, T Yamada, I Kawagishi, Y Imae, and M Homma, 1996,*J. Bacteriol.*, vol. 178, no. 16, 5024-5026.
[8] H C Berg, *Random Walks in Biology*, Princeton, New Jersey, USA: Princeton University Press, **1993**.
[9] B Behkam, M Sitti, **2007**, *Appl. Phys. Lett.*, vol. 90, no. 2.
[10] S Martel, **2012**, *Biomed. Microdevices*, vol. 14, 1033-145.
[11] H.C. Berg, L. Turner, **1990**,*Biophys J*, 58, 919.
[12] Z. Liu, K.D. Papadopoulos, 1995, *Appl. Environ. Microbiol.*, vol. 61, no. 10, 3567-3572.
[13] S.A. Biondi, J.A. Quinn, H. Goldfine, **1998**, *AIChE Journal*, vol. 44, no.8, 1923-1929.
[14] W.R. DiLuzio, L.Turner, M.Mayer, P.Garstecki, D.B. Weibel, H.C. Berg, G.M. Whitesides, **2005**,*Nature*, 435,30, 1271-4.
[15] G. Li, L.-K. Tam, and J. X. Tang, **2008**, *Proc. Natl. Acad. Sci. PNAS*, vol. 105, no. 47, 18355-18359.
[16] M. R. Edwards, R. W. Carlsen, and M. Sitti, **2013**,*Appl. Phys. Lett.*, vol. 102, 143701-4,.
[17] B. U. Felderhof, **2010**, *Phys of Fluids*, vol. 22, 1136041-6.
[18]J. J. Higdon, **1979**, *J. Fluid Mech.*, vol. 94, no. 2, 331-351.
[19]D. J. Smith, E. A. Gaffney, J. R. Blake, and J. C. Kirkman-Brown, **2009**,*J. Fluid Mech.*, vol. 621, 289-320.